Dielectric functions of $In_xGa_{1-x}As$ alloys

T. J. Kim,[1] T. H. Ghong,[1] Y. D. Kim,[1,*] S. J. Kim,[2] D. E. Aspnes,[2] T. Mori,[3] T. Yao,[3] and B. H. Koo[4]
[1]*Department of Physics and Research Institute for Basic Sciences, Kyung Hee University, Seoul 130-701, Korea*
[2]*Department of Physics, North Carolina State University, Raleigh, North Carolina 27606, USA*
[3]*Center for Interdisciplinary Research, Tohoku University, Sendai 980-8578, Japan*
[4]*Department of Ceramic Science and Engineering, Changwon National University, Gyeongnam 641-773, Korea*
(Received 8 January 2003; revised manuscript received 4 June 2003; published 29 September 2003)

We present room-temperature pseudodielectric function spectra $\langle\varepsilon\rangle=\langle\varepsilon_1\rangle+i\langle\varepsilon_2\rangle$ of $In_xGa_{1-x}As$ films grown on (100) InP by solid-source molecular-beam epitaxy. A wet-chemical etching procedure was used to remove overlayers and obtain the best approximation to the bulk dielectric responses $\varepsilon=\varepsilon_1+i\varepsilon_2$ of the films. By lineshape fitting we determined the dependences of the $E_1, E_1+\Delta_1, E_0', E_0'+\Delta_0'$, and E_2 critical-point energies on x. Using a parametric semiconductor model we represent these spectra analytically to allow $\langle\varepsilon\rangle$ to be calculated as a continuous function of x. These results are expected to be useful for design purposes, for example of nanostructures and multilayer systems involving $In_xGa_{1-x}As$.

DOI: 10.1103/PhysRevB.68.115323 PACS number(s): 78.20.Ci, 78.40.Fy, 78.66.Fd

I. INTRODUCTION

The $In_xGa_{1-x}As$ alloys have attracted much attention because selected compositions can outperform GaAs with respect to electron transport and their room-temperature bandgaps are particularly well suited for applications involving infrared emitting diodes and detectors.[1] However, for many purposes accurate values of the dielectric functions $\varepsilon=\varepsilon_1+i\varepsilon_2$ of the bulk material are needed as a continuous function of In composition x, for example for bandgap engineering, optimizing properties for specific device applications, *in situ* monitoring of the growth of $In_xGa_{1-x}As$ alloys, and *ex situ* characterization of interfaces in nanostructured or multilayered materials. Even though extensive optical studies have been performed on nearly lattice-matched $In_xGa_{1-x}As$ films grown on InP substrates[2] and SE data on strained InGaAs films[3] have been reported, to our knowledge very little data are available on $In_xGa_{1-x}As$ alloy films over entire composition range,[4,5] and no previous work has been done to parametrize these data as a continuous function of x.

In this paper we present the results of a spectroscopic ellipsometric determination of the room-temperature pseudodielectric functions $\langle\varepsilon\rangle=\langle\varepsilon_1\rangle+i\langle\varepsilon_2\rangle$ and interband transition energies of $In_xGa_{1-x}As$ alloys for eight values of x, including the endpoint values $x=0$ and $x=1$, and provide the parameters that allow $\langle\varepsilon\rangle$ to be calculated as a function of x over the entire range. The pseudodielectric function is that quantity calculated from the ellipsometrically determined complex reflectance ratio ρ in the two-phase (substrate/ambient) model without regard for surface overlayers, and reduces to ε if overlayer effects are negligible. Spectroscopic ellipsometry[6–13] (SE) is an excellent technique for determining dielectric function data, since these can be obtained directly from ρ without the need of Kramers-Kronig transformations. In addition, its nondestructive nature and high surface sensitivity allows surface conditions to be assessed and optimized in real time, thereby ensuring that $\langle\varepsilon\rangle$ approximates ε as closely as possible. We approached this objective by performing the chemical etching procedure described below to remove physisorbed contaminant and natural oxide overlayers. Such etching procedures have been found to reduce the broadening of critical-point (CP) structures in the region of the E_2 peak in other materials.[14,15] another indication of higher surface quality. CP energies obtained by lineshape fitting show that the E_1 structures $(E_1, E_1+\Delta_1)$ exhibit a positive bowing and a redshift with increasing x. The E_2 structures $(E_0', E_0'+\Delta_0', E_2)$ also exhibit a redshift with increasing x.

To obtain analytic expressions giving $\langle\varepsilon\rangle$ as continuous functions of composition and photon energy, we represent these data as sums of energy-bounded, Gaussian-broadened polynomials and poles.[16] This allows our results to be extended to arbitrary x and provides an analytic database for various purposes including those listed above.

II. EXPERIMENTAL

Our $In_xGa_{1-x}As$ films were grown on (001) semi-insulating InP substrates by solid-source molecular beam epitaxy. The substrate temperature during growth was monitored by IR pyrometry. The native oxide overlayers were thermally removed at 530 °C under As. 1 μm thick $In_xGa_{1-x}As$ layers of In compositions x from 0.00 (GaAs) to 0.66 were grown at 510 °C at a rate of 0.6 μm/h. During deposition the surfaces showed a streaky reflection high energy electron diffraction (RHEED) pattern, indicating two-dimensional growth.

The compositions of the layers were determined by high-resolution x-ray diffraction. The uncertainty of HRXRD is estimated to be about 3%, which as an example translates to about 0.01 for $x = 0.34$. This uncertainty is smaller than the dot size in the following figures.

According to information provided in Refs. 17 and 18, 1 μm greatly exceeds the critical thicknesses of strain relaxation for all films studied here, with the possible exception of that for $x=0.52$. For example for $x=0.49$ and 0.56 the critical thicknesses are 447 and 732 Å, respectively. For $x=0.52$ the critical thickness is 2056 Å, but in this case any residual strain effects will be small. Therefore, we believe that all data presented here are representative of bulk responses even though we did not perform HRXRD profile measurements explicitly.

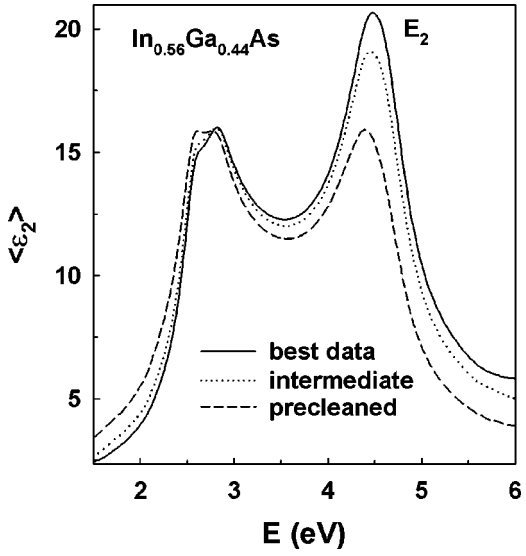

FIG. 1. Imaginary part of $\langle\varepsilon\rangle$ as a function of chemical treatment for a $In_{0.56}Ga_{0.44}As$ film. Dashed, dotted, and solid lines represent pretreated, intermediate, and best final data, respectively.

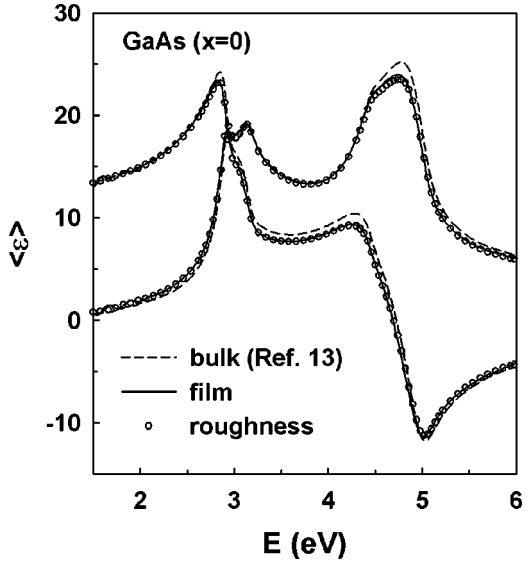

FIG. 2. Comparison of the $\langle\varepsilon\rangle$ spectrum of GaAs obtained on a relaxed film (solid line) with that reported in Ref. 13 for bulk material (dashed line). The difference can be modeled (open circles) as 7.2 Å of surface roughness.

$\langle\varepsilon\rangle$ spectra were obtained from 1.5 to 6.0 eV using an automatic spectroscopic rotating-analyzer ellipsometer.[6] These data were obtained with the samples were at room temperature. Light from a 75 W xenon lamp was dispersed by a monochromator and linearly polarized with a Rochon prism. The properties of the elliptically polarized light that resulted when this beam was reflected from the sample were determined by modulating the reflected beam with a rotating Rochon prism and detecting it with a photomultiplier. Measurements were performed at an incident angle of 67.08°.

It is well known that the existence of overlayers on a surface complicates efforts to obtain e by SE because of its surface sensitivity.[19] We minimized overlayer artifacts by following the wet-chemical etching procedure described in Refs. 15 and 20. Figure 1 shows the results of the chemical etching treatment of $In_{0.56}Ga_{0.44}As$ as an example. Successive applications of a 1:5 mixture of NH_4OH and methanol, BrM (a 0.05% solution of bromine in methanol), deionized (DI) water, and methanol were repeated until the $\langle\varepsilon_2\rangle$ spectra showed no further changes, and the highest values of $\langle\varepsilon_2\rangle$ in the region of the E_2 bandgap near 4.5 eV were obtained. The highest value imply the most abrupt interface[19] and therefore that the associated spectrum is the best representation of the intrinsic dielectric function that this procedure can achieve.

Despite these precautions the data still appear to be af-

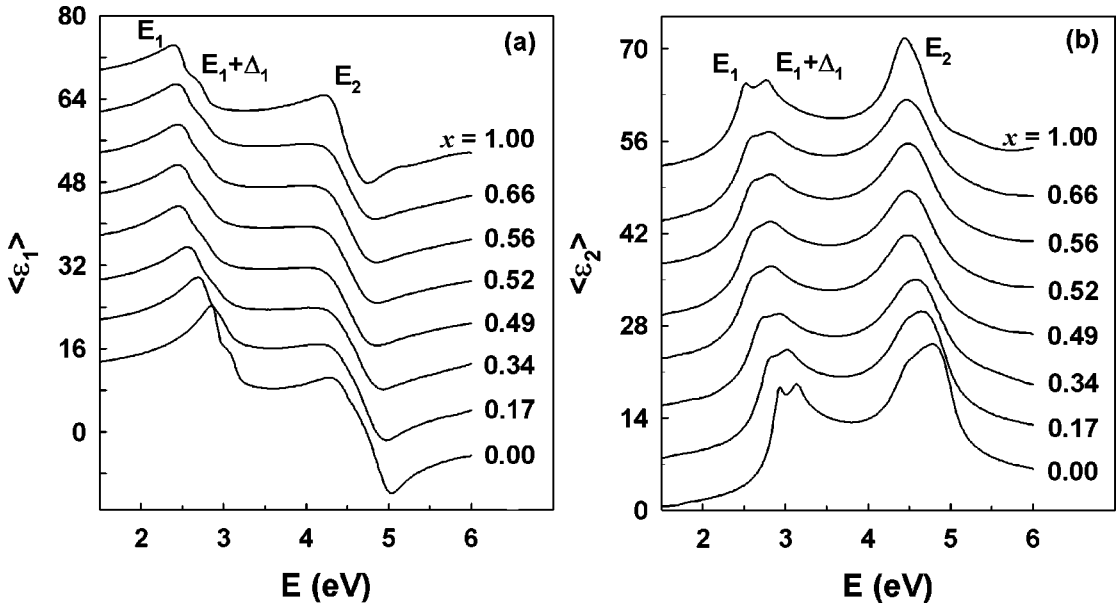

FIG. 3. Real (a) and imaginary (b) parts of $\langle\varepsilon\rangle$ of $In_xGa_{1-x}As$ at room temperature for $x=$ 0.00, 0.17, 0.34, 0.49, 0.52, 0.56, 0.66, and 1.00. Successive spectra are offset by 8 and 7 in (a) and (b), respectively.

fected by residual roughness and possibly to a small extent by residual strain. The evidence for residual roughness is given in Fig. 2, where we compare $\langle\varepsilon\rangle$ data for GaAs obtained on a relaxed film (solid lines) with that previously reported for bulk material (dashed lines) using the same ellipsometer and measurement procedure.[13] The difference can be modeled rather accurately by a 7.2 Å thick layer of surface roughness (open circles), possibly due to local differences in etch rates near dislocations resulting from lattice relaxation. Strain effects have previously been observed in the analysis of data for SiGe alloys[21] on different substrates. If GaAs could be grown pseudomorphically on InP the result would be a blue shift of 270 meV from the information given in Ref. 22. However, we observe a slight ($\sim$10 meV) redshift in the CP energies of the E_1 and $E_1+\Delta_1$ transitions for the GaAs film. This can be understood as a result of the distortion of the $\langle\varepsilon\rangle$ spectra by surface roughness, which we confirmed by a multilayer model calculation. For InGaAs alloys the film-bulk comparison suggests strain effects of the order of 10 meV on the critical point energies. Unfortunately, these uncertainties will not be resolved until bulk InGaAs alloys become available. The complete assessment of these effects is beyond our present capabilities, so these uncertainties will remain until $\langle\varepsilon\rangle$ spectra can be obtained on bulk InGaAs samples.

III. RESULTS AND DISCUSSIONS

A. $In_xGa_{1-x}As$ dielectric functions

$\langle\varepsilon_1\rangle$ and $\langle\varepsilon_2\rangle$ spectra of $In_xGa_{1-x}As$ alloys for $x=0.0$ (GaAs), 0.17, 0.34, 0.49, 0.52, 0.56, 0.66, and 1.0 (InAs) are shown in Figs. 3(a) and 3(b), respectively. The spectra are offset by increments of 8 and 7 for the real and imaginary parts, respectively, relative to the bottom spectrum ($x=0.0$). The GaAs and InAs spectra are those previously reported for bulk material, as discussed above.[13] We use these bulk spectra instead of our film data because one of our goals is to obtain the most accurate possible representation of $\langle\varepsilon\rangle$ for modeling purposes. The shift of the three main peaks E_1,$E_1+\Delta_1$, and E_2 to lower energies with increasing x is easily seen. The E_1 and $E_1+\Delta_1$ structures in the $\langle\varepsilon_2\rangle$ spectra are highly resolved at $x=0.0$ but lose their sharpness up to $x\sim0.5$ then regain it as the other end point $x=1.0$ is

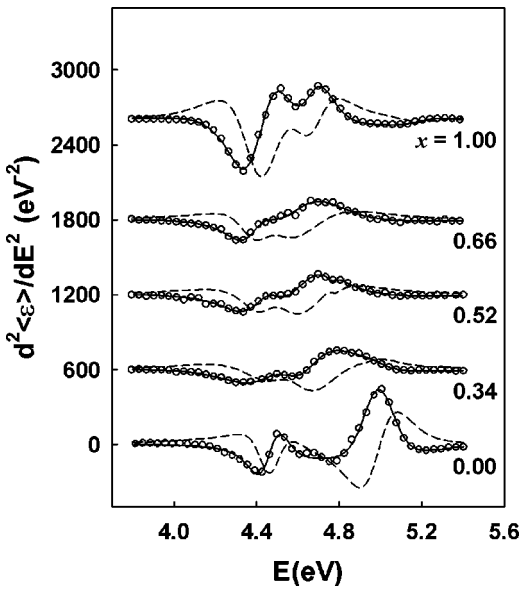

FIG. 5. Fits to the second energy derivatives of $\langle\varepsilon_1\rangle$ (solid line) and $\langle\varepsilon_2\rangle$ (dashed line) of $In_xGa_{1-x}As$ in the E_2 spectral region. The dots represent data for $d^2\langle\varepsilon_1\rangle/dE^2$. For clarity the data are shown only for $\langle\varepsilon_1\rangle$, and the number of points is reduced by half. Critical point energies are indicated by arrows. Successive spectra are offset by 600 from the bottom $x=0.0$, except for the top $x=1.0$, which is offset by 800.

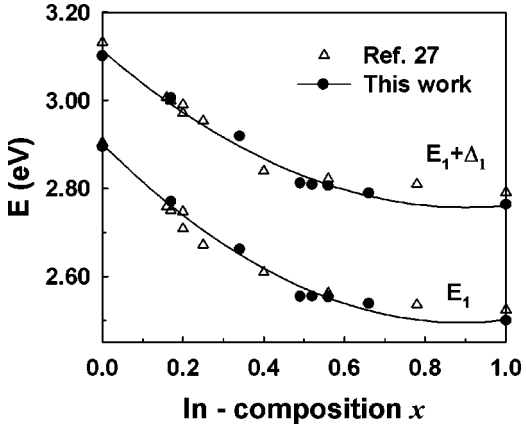

FIG. 4. Dependences of CP energies of $In_xGa_{1-x}As$ on composition x for the E_1 and $E_1+\Delta_1$ transitions. Solid circles represent the data obtained here, while open triangles are from Ref. 27. The solid lines indicate the best fits to our data with $E(x)=ax^2+bx+c$.

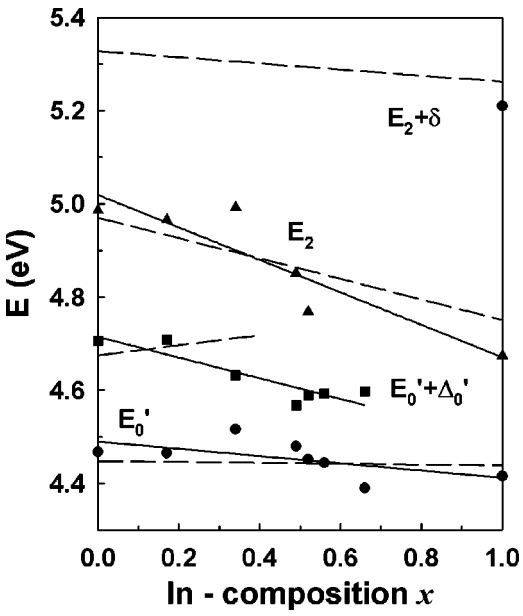

FIG. 6. Dependence of critical-point energies of $In_xGa_{1-x}As$ on x in the region of the E_2 peak. The dots show the results of our line shape analysis. The solid lines are the best fits of these energies to a straight line. The dashed lines show the dependence obtained by Thompson *et al.* (Ref. 29).

approached. This broadening dependence is simply due to statistical fluctuations of the crystal potential in the alloys,[23,24] which should significantly exceed any possible contribution from bulk dislocations.

B. E_1 peak region

To obtain the x dependence of the CP energies, we fit the standard analytic CP expressions[25,26]

$$\frac{d^2\varepsilon}{d\omega^2}=\begin{cases} n(n-1)Ae^{i\phi}(\omega-E+i\Gamma)^{n-2}, & n\neq 0, \\ Ae^{i\phi}(\omega-E+i\Gamma)^{-2}, & n=0 \end{cases} \quad (1)$$

to numerically calculated second-energy-derivative spectra. Here, the exponent n has the values $-1,-1/2,0$, and $1/2$ for excitonic, one-, two-, and three-dimensional CP's, respectively. Both real and imaginary parts were fit simultaneously. Details of the analysis were reported previously.[5] Figure 4 shows the fitted CP energies (solid circles) compared to values obtained from electroreflectance (ER) measurements (open triangles).[27] Since the ER measurements were not made under low-field conditions, the present results are more accurate. The solid lines show the fit of our data to the quadratic $E(x)=ax^2+bx+c$.

TABLE I. Parameters of the E_0', $E_0'+\Delta_0'$, and E_2 critical points in $E(x)=bx+c$. The uncertainties correspond to 95% confidence limits.

	E_0'	$E_0'+\Delta_0'$	E_2
b	-0.08 ± 0.041	-0.22 ± 0.046	-0.35 ± 0.078
c	4.49 ± 0.022	4.71 ± 0.021	5.02 ± 0.041

The best-fit coefficients a, b, and c are listed in Table I of Ref. 5. The fact that the best-fit lines essentially go through the endpoints without additional constraints gives an additional measure of confidence in the CP energies determined in this way.

C. E_2 peak region

Figure 5 shows numerically calculated second energy derivatives in the region of the E_2 peak. These derivatives were calculated to assist in obtaining the x dependences of the different CP energies in this range. The open circles represent the calculated values of the real part of $d^2\varepsilon/d\omega^2$. For clarity only half the points for $\langle\varepsilon_1\rangle$ and none for $\langle\varepsilon_2\rangle$ are shown. The results were fit to a 3-CP version of Eq. (1), yielding best-fit values as the solid and dashed lines.

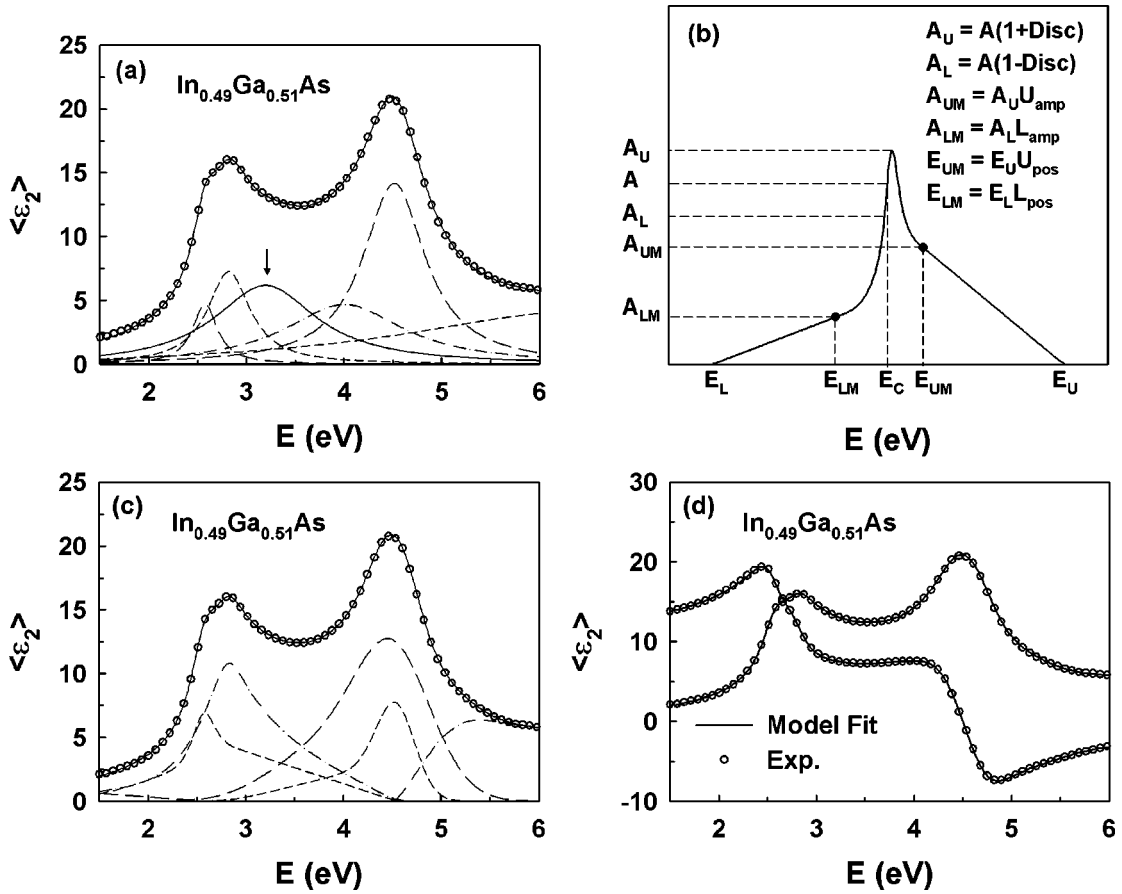

FIG. 7. (a) Representation of the dielectric response of the $In_{0.49}Ga_{0.51}As$ film by the Lorentz oscillator model, which requires a physically unreasonable bandgap of 3.26 eV as indicated by the arrow. (b) A single CP structure described by the parametric model with four polynomial ensembles. (c) As (a), but with the parametric model. (d) As (c), but for real and imaginary parts. The open circles are data and the solid lines are the best fits to these data.

Figure 6 represents the x dependence of the CP energies in the E_2 region. The solid circles (E_0'), squares ($E_0'+\Delta_0'$), and triangles (E_2) are from the fits shown in Fig. 5. Given the scatter caused by the fact that these structures significantly overlap each other we concluded that nothing would be gained by attempting a quadratic fit, so we assumed a linear variation $E(x)=bx+c$. This is consistent with previous analyses done in this spectral region for many other semiconductor alloys.[7,8,28] The solid lines correspond to these best fits. The values of b and c for the $E_0', E_0'+\Delta_0'$, and E_2 structures are listed in Table I. The values of c are the CP energies of GaAs, which correspond to reported values.

A comparison of our data with those of Ref. 29 (dashed lines) is also shown in Fig. 6. We could not resolve the $E_2+\delta$ structure when $x<1.0$, so no line is associated with this CP. It is interesting to note that the slope of the $E_0'+\Delta_0'$ peak is negative in our data, while it is positive in Ref. 29. Since the ER data of Ref. 29 were also not obtained under low-field conditions, we again place more weight on the SE results. Therefore, we believe that the $E_0'+\Delta_0'$ line should have a negative slope. We note that the application of different lineshape models leads to different CP energy values when adjacent CP's have large overlap, as is the case in the E_2 region. However, as we will show in the next section, a different approach gives the same negative slope. This interpretation is also supported by the fact that the E_0' and $E_0'+\Delta_0'$ CP's should exhibit similar behavior since they occur at the same place in the Brillouin Zone. However, for a precise understanding and identification of these structures, further theoretical calculations of the band structure of these alloys are needed.

D. Modeling of $In_xGa_{1-x}As$ alloy spectra

To obtain dielectric functions of $In_xGa_{1-x}As$ alloys for arbitrary x, we first tried a conventional Lorentz-oscillator model[30–32] for $In_{0.49}Ga_{0.51}As$. The result for the $\langle\varepsilon_2\rangle$ spectrum is shown in Fig. 7(a) as an example. The solid line represents the data (open circles) very well with a chi-squared value of 3.1577. However, to smoothly connect the E_1- and E_2-peak regions, a physically unreasonable bandgap of 3.26 eV is needed.

We therefore used the parametric semiconductor model.[16] This approach begins with the treatment used to derive the parametric dispersion[33] and nearly all other oscillator-type dispersion models.[31] Detailed explanations of the model are provided in Refs. 16, 34, and 35. In brief, the dielectric function of parametric model is written as the summation of m energy-bounded, Gaussian-broadened polynomials and P poles accounting for index effects due to absorption outside the model region:[16,34,35]

$$\begin{aligned}\varepsilon(\omega)&=\varepsilon_1(\omega)+i\varepsilon_2(\omega)\\&=1+i\sum_{j=1}^{m}\int_{E_{\min}}^{E_{\max}}W_j(E)\Phi(\hbar\omega,E,\sigma_j)dE\\&\quad+\sum_{j=m+1}^{m+P+1}\frac{A_j}{(\hbar\omega)^2-E_j^2},\end{aligned}\tag{2}$$

where

$$\begin{aligned}\Phi(\hbar\omega,E,\sigma_j)&=\int_0^\infty e^{i(\hbar\omega-E+i2\sigma^2 s)s}ds\\&\quad-\int_0^\infty e^{i(\hbar\omega+E+i2\sigma^2 s)s}ds\\&=\sqrt{\frac{\pi}{8\sigma^2}}[e^{-y_1^2}+e^{-y_1^2}\mathrm{erf}(iy_1)\\&\quad-e^{-y_2^2}-e^{-y_2^2}\mathrm{erf}(iy_2)],\end{aligned}\tag{3a}$$

$$y_1=\frac{\hbar\omega-E}{2\sqrt{2}\sigma}\ \text{ and }\ y_2=\frac{\hbar\omega+E}{2\sqrt{2}\sigma},\tag{3b}$$

$$W_j(E)=\sum_{k=0}^{N}P_{j,k}E^k u(E-a_j)u(b_j-E),\tag{3c}$$

TABLE II. The entire set of parameters for $In_{0.49}Ga_{0.51}As$ for in the parametric model. Blank entries represent parameters that are not used. Parameters denoted by asterisks are assumed to be independent of x. Uncertainties refer to 90% confidence levels.

No	con$L$	con$U$	E	A	Γ	Disc.	Lpos	Lamp	L2nd	Upos	Uamp	U2nd
♯0	0	1	0.76	0.5*	20*	0*	0.5*	0.5*	0*	0.4*	0.75*	0*
♯1	0	3	2.54	8.80	82.55	0.2*	0.74*	0.28	1*	0.8*	0.4*	0*
			±0.0017	±0.27	±3.18			±0.0031				
♯2	0	3	2.86	11.90	96.55	−0.1*	0.3*	0.05*	0*	0.1*	0.066	0*
			±0.0032	±0.20	±0.30						±0.0014	
♯3	2	5	4.51	35.33	407.36	−0.17*	0.7*	0.15	0*	0.9*	0.4*	0*
			±0.0055	±0.36	±12.89			±0.0068				
♯4	2	5	4.59	23.52	231.80	−0.99*	0.8*	0.06*	0*	0.5*	0.5*	0*
			±0.0016	±0.19	±3.27							
♯5	3	6	5.57	4.84	25.20	0*	0.5*	0.53	0*	0.5*	0.76	0*
			±0.016	±0.067	±37.53			±0.0032			±0.011	
♯6			10*									

TABLE III. Parameters of the parametric model for all $In_xGa_{1-x}As$ alloys. Uncertainties refer to 90% confidence levels.

x	0.00	0.17	0.34	0.49	0.52	0.56	0.66	1.00
E_0	1.430	1.166	0.936	0.761	0.729	0.688	0.594	0.350
E_1	2.891	2.751	2.652	2.544	2.541	2.546	2.521	2.476
	± 0.0014	± 0.0016	± 0.0016	± 0.0017	± 0.0025	± 0.0018	± 0.0014	± 0.0021
$A(E_1)$	3.163	8.655	9.361	8.800	8.936	9.849	9.208	9.949
	± 0.27	± 0.36	± 0.35	± 0.27	± 0.43	± 0.30	± 0.24	± 0.22
$\Gamma(E_1)$	4.592	59.373	78.277	82.553	88.720	86.076	83.266	48.385
	± 2.86	± 3.57	± 3.43	± 3.18	± 4.13	± 3.36	± 2.66	± 3.96
$L\mathrm{amp}(E_1)$	4.924	0.222	0.278	0.284	0.273	0.292	0.260	0.310
	± 0.0029	± 0.0027	± 0.0033	± 0.0031	± 0.0027	± 0.0032	± 0.0020	± 0.0040
$E_1+\Delta_1$	5.770	3.032	2.952	2.860	2.858	2.868	2.844	2.811
	± 0.0025	± 0.0038	± 0.0043	± 0.0032	± 0.0050	± 0.0035	± 0.0030	± 0.0029
$A(E_1+\Delta_1)$	12.186	14.181	11.735	11.905	11.579	11.076	11.076	10.912
	± 0.20	± 0.28	± 0.27	± 0.20	± 0.31	± 0.22	± 0.18	± 0.17
$\Gamma(E_1+\Delta_1)$	12.965	114.907	117.211	96.533	101.279	89.555	103.346	52.140
	± 4.35	± 3.93	± 4.40	± 3.30	± 4.94	± 3.93	± 3.34	± 5.30
$U\mathrm{amp}(E_1+\Delta_1)$	41.226	0.049	0.056	0.066	0.066	0.064	0.061	0.043
	± 0.0011	± 0.0010	± 0.0017	± 0.0014	± 0.0022	± 0.0017	± 0.0014	± 0.0018
E_0'	22.489	4.572	4.565	4.512	4.513	4.520	4.520	4.546
	± 0.0050	± 0.0042	± 0.0050	± 0.0055	± 0.0083	± 0.0056	± 0.0046	± 0.023
$A(E_0')$	6.224	38.960	35.930	35.329	35.376	35.807	34.425	26.522
	± 0.66	± 0.40	± 0.42	± 0.36	± 0.043	± 0.60	± 0.29	± 1.22
$\Gamma(E_0')$	35.128	244.756	318.916	407.362	411.345	394.535	388.575	340.320
	± 3.19	± 3.07	± 9.71	± 12.89	± 18.73	± 14.55	± 12.50	± 30.04
$L\mathrm{amp}(E_0')$	50.539	0.207	0.191	0.155	0.152	0.158	0.161	0.150
	± 0.0028	± 0.0028	± 0.0053	± 0.0068	± 0.0100	± 0.0080	± 0.0062	± 0.0100
$E_0'+\Delta_0'$	206.579	4.833	4.706	4.594	4.593	4.594	4.581	4.551
	± 0.0021	± 0.0037	± 0.0069	± 0.0016	± 0.0022	± 0.0017	± 0.0013	± 0.0016
$A(E_0'+\Delta_0')$	159.455	16.896	17.421	23.521	22.683	21.685	20.834	30.441
	± 0.91	± 0.68	± 1.22	± 1.19	± 1.65	± 1.31	± 1.15	± 2.89
$\Gamma(E_0'+\Delta_0')$	61.104	193.176	228.056	231.795	230.130	222.688	219.187	194.310
	± 3.25	± 3.86	± 3.92	± 3.27	± 4.74	± 3.76	± 3.42	± 6.45
E_2	0.201	5.731	5.686	5.573	5.565	5.475	5.511	5.434
	± 0.017	± 0.0083	± 0.022	± 0.016	± 0.0075	± 0.024	± 0.0050	± 0.017
$A(E_2)$	0.042	5.733	5.152	4.836	4.767	4.988	4.715	4.756
	± 0.047	± 0.028	± 0.06	± 0.067	± 0.095	± 0.085	± 0.063	± 0.13
$\Gamma(E_2)$	0.184	29.680	23.633	25.196	33.879	29.777	32.673	135.014
	± 25.55	± 27.13	± 50.04	± 37.53	± 50.84	± 0.038	± 30.28	± 34.00
$L\mathrm{amp}(E_2)$	0.474	0.501	0.529	0.529	0.528	0.534	0.542	0.667
	± 0.0086	± 0.0051	± 0.0058	± 0.0032	± 0.0047	± 0.0058	± 0.0035	± 0.033
$U\mathrm{amp}(E_2)$	0.622	0.653	0.719	0.762	0.775	0.724	0.771	0.782
	± 0.0060	± 0.0040	± 0.0087	± 0.011	± 0.016	± 0.013	± 0.011	± 0.024

where $u(x)$ is the unit step function. The use of pure Gaussian broadening in Eq. (3a) essentially prohibits closed-form integration of Eq. (2). However, the equivalent expression shown in Eq. (3b) shows that one-dimensional lookup tables as a function of $(\hbar\omega+E)/(2\sqrt{2}\sigma)$ can be constructed numerically for each order of polynomial required by Eq. (3c).

In the specific implementation for this work, the polynomials are grouped into four polynomial ensembles with fourth order polynomials [$N=4$ in Eq. (3)], which are centered on critical point structures with the overlapping tails of adjacent ensembles filling in the intervening absorption regions, as depicted in Fig. 7(b). The center energies E_C correspond to the CP energies, while the bounding energies E_L and E_U delineate adjacent CP's. The positions of the two control points E_{LM} and E_{UM}, which correspond to the joining points of the four polynomials, are defined relative to these CP energies via relations in Eq. (3b). At the E_C discontinuities in amplitude and energy are permitted; hence the two sides of the ensemble are independent and step-like absorption features can be created to model direct bandgaps.

Figure 7(c) shows the improved representation obtained by this model, which results in a more accurate reproduction

TABLE IV. Composition dependence of the parameters in Table III as approximated by the quadratic $f(x)=ax^2+bx+c$. Uncertainties refer to 95% confidence levels.

param	a	b	c	param	a	b	c
E_0	0.56 ± 0.0021	-1.64	1.43	E_0'	0.17 ± 0.0243	-0.22	4.59
E_1	0.49 ± 0.0215	-0.91	2.89	$A(E_0')$	-6.82 ± 1.8342	-7.89	41.23
$A(E_1)$	8.51 ± 1.5347	-10.75	12.19	$\Gamma(E_0')$	-436.56 ± 45.9261	570.30	206.58
$\Gamma(E_1)$	-173.88 ± 3.3783	187.14	35.13	$L\text{amp}(E_0')$	0.001 ± 0.0271	-0.03	0.18
$L\text{amp}(E_1)$	-0.08 ± 0.0284	0.19	0.20	$E_0'+\Delta_0'$	0.48 ± 0.0377	-0.85	4.92
$E_1+\Delta_1$	0.45 ± 0.021	-0.80	3.16	$A(E_0'+\Delta_0')$	23.74 ± 4.0467	-15.79	22.49
$A(E_1+\Delta_1)$	0.96 ± 1.2573	-3.01	12.97	$\Gamma(E_0'+\Delta_0')$	-204.51 ± 11.1656	239.36	159.45
$\Gamma(E_1+\Delta_1)$	-224.28 ± 28.5991	225.88	50.54	E_2	0.13 ± 0.0701	-0.47	5.77
$U\text{amp}(E_1+\Delta_1)$	-0.08 ± 0.0055	0.08	0.04	$A(E_2)$	2.37 ± 0.1611	-3.84	6.22
				$\Gamma(E_2)$	293.74 ± 9.793	-219.83	61.10
				$L\text{amp}(E_2)$	0.16 ± 0.0272	0.03	0.47
				$U\text{amp}(E_2)$	-0.18 ± 0.0334	0.34	0.62

of the $\langle\varepsilon_2\rangle$ data as shown by the smaller chi-square deviation of 1.9058. It also shows that there is no need for fictitious oscillators that serve only to fill in gaps, as required when using Lorentz or harmonic-oscillator models. Table II shows the best-fit parameters obtained for $In_{0.49}Ga_{0.51}As$, where con$L$ and con$U$ specify the neighboring CP points to give the values of E_L and E_U, respectively. Figure 7(d) shows the actual fit for both real and imaginary parts of $\langle\varepsilon\rangle$, where the lines are the model and the open circles the data. The uncertainty of the linewidth of the E_2 peak is large, which can be understood by reference to Fig. 7(c). This peak has a broad tail extending well above our measurement limit of 6 eV, and therefore the actual value of Γ has little effect. The same argument applies in Table III below.

For each available sample $x=0.0$, 0.17, 0.34, 0.49, 0.52, 0.56, 0.66, and 1.0 a similar fit was performed. The entire set of parameters used to model these $In_xGa_{1-x}As$ dielectric functions is given in Table III. Parameters that are not listed in Table III are fixed-value ones that are the same as those for the $In_xGa_{1-x}As$ alloy,and are shown in Table II with an asterisk. By interpolating the results given in Tables II and III we can construct numerical values of $\langle\varepsilon\rangle$ for arbitrary compositions. To accomplish this the x-dependence of each parameter given in Table III was obtained by fitting to it the quadratic equation $f(x)=ax^2+bx+c$. Since the two end points are reference bulk values, we used only a single free parameter a in fitting procedure. The resulting coefficients a,b, and c of the quadratics associated with each parameter are listed in Table IV.

Figures 8(a) and 8(b) show the x dependences of linewidths and midpoint amplitudes as examples. It is interesting to note that the linewidth of the E_2 peak has a physically absurd positive bowing instead of the negative bowing for the general cases, which is probably a result of the param-

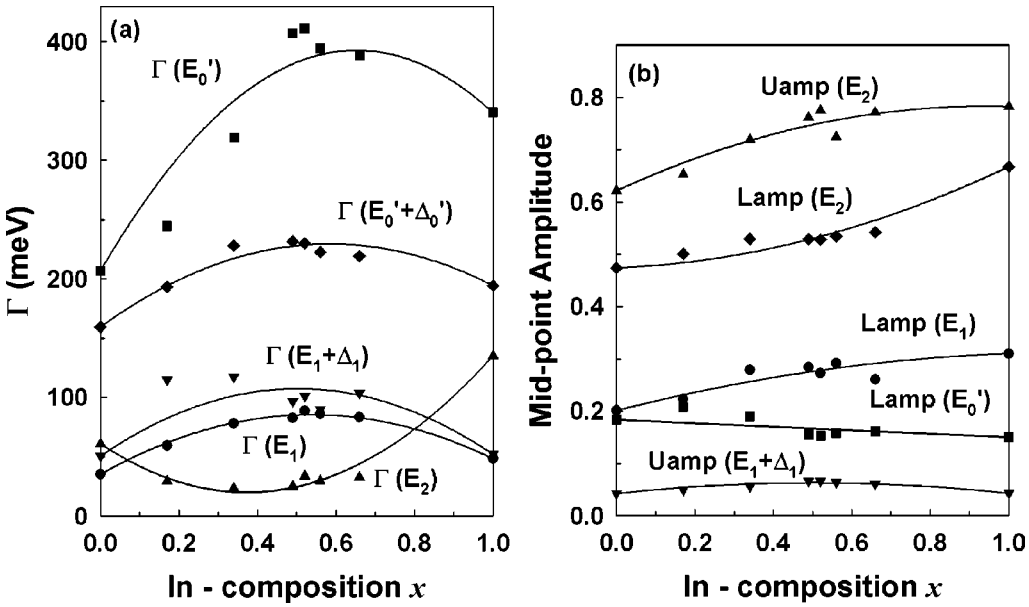

FIG. 8. Composition dependences of some CP linewidths (a) and amplitudes (b). The dots are calculated parameters and the lines are quadratic fits.

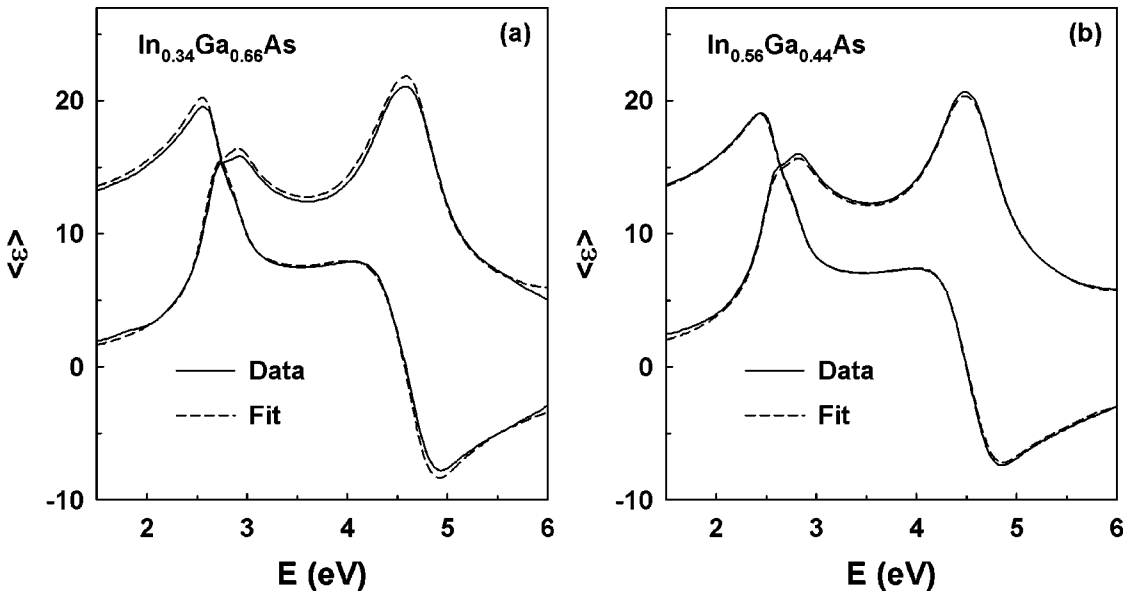

FIG. 9. Comparison of data (solid lines) with spectra (dashed lines) reconstructed from the parameters of Table IV for $x=0.34$ (a) and $x=0.56$ (b).

eters adjusting to give the best possible representation of $\langle\varepsilon\rangle$.

The resulting dielectric functions of several In composition x are shown in Fig. 9. From these results spectra of arbitrary x can be calculated for use in various tasks, for example the characterization of interfaces in nanostructured or multilayered materials.

E. Comments

An interesting test is the capability of the model to reconstruct the original $\langle\varepsilon\rangle$ data, since the parameters show some scatter about the best-fit lines. Figures 10(a) and 10(b) show the comparisons for $x=0.34$ and 0.56, respectively. The former exhibits the biggest difference between the measured and calculated spectra. Remaining spectra show differences similar to that seen in Fig. 10(b), where the agreement is acceptable. We estimate that in multilayer calculations involving this database the uncertainties in computed thicknesses would be less than 4 Å

It is also interesting to compare the CP energies obtained from the derivative spectra of Eq. (1) with those obtained from the parametric model spectra. To confirm the negative slope of the $E_0'+\Delta_0'$ peak in Fig. 6, we plot in Fig. 11 the CP energies obtained by three different methods. ''Eq. (1)'' (solid circles) refers to the standard method of fitting Eq. (1) to the second numerical derivative of the data of Fig. 2, and simply reproduces the values plotted in Figs. 4 and 6. ''PM''

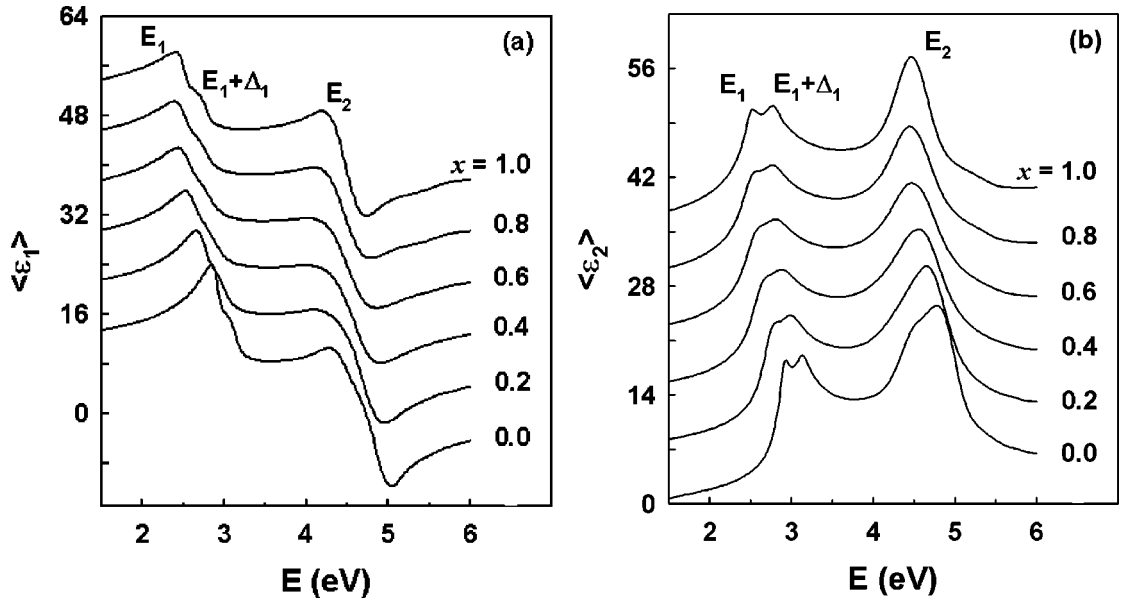

FIG. 10. Real (a) and imaginary (b) parts of $\langle\varepsilon\rangle$ of $In_xGa_{1-x}As$ for $x=0.0$, 0.2, 0.4, 0.6, 0.8, and 1.0 calculated in the parametric representation.

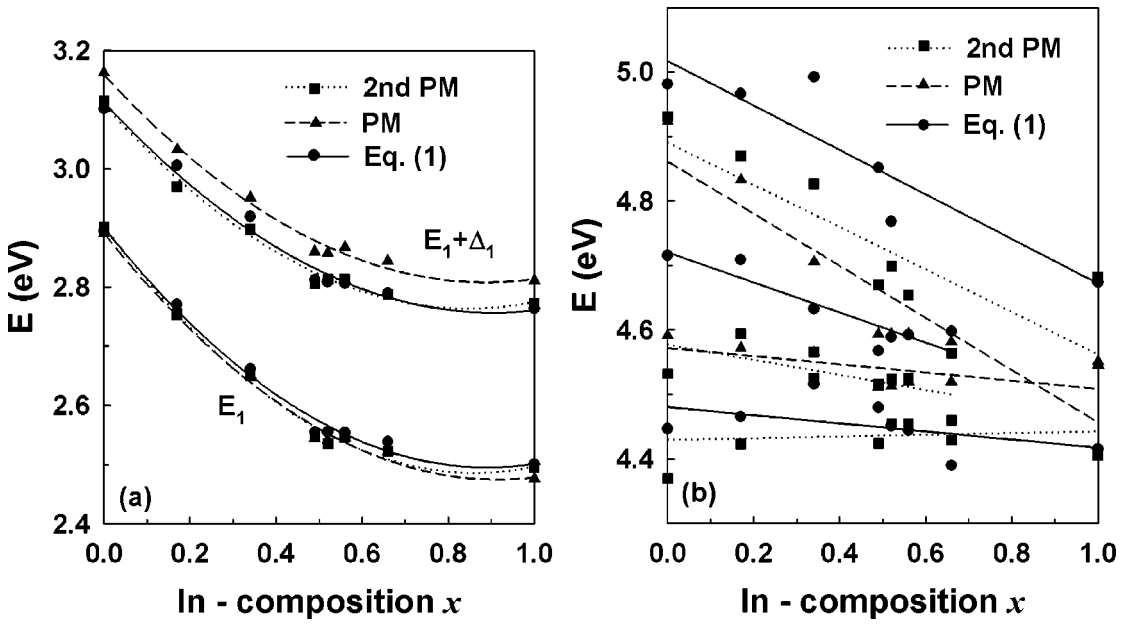

FIG. 11. Composition dependences of CP energies in the (a) E_1 and (b) E_2 peak regions obtained as described in the text. The solid, dashed, and dotted lines are best fits to the different calculations.

(solid triangles) represents the CP energies listed in Table III. These were obtained from a least-squares fit to the parameters determined for specific x from Eq. (1). The second PM (solid squares) was obtained by fitting Eq. (1) to the second numerical derivatives of spectra calculated from the parametric model. The solid, dashed, and dotted lines are least-squares fits of a quadratic to these values, respectively. The results for the E_1 structure, which is well separated and has a small linewidth, are essentially independent of the analysis method. However, the $E_1+\Delta_1$ peak, which has a large linewidth, and the E_2 region, which shows considerable overlapping of critical points, exhibit strong model dependences. By convention the method based on Eq. (1) is widely accepted and agrees with other measurements. Consequently, we conclude that, of the three approaches used here, the values obtained in this way are the most reliable. We emphasize that the slope of the $E_0'+\Delta_0'$ CP in Fig. 11(b) is clearly negative in all cases.

IV. CONCLUSIONS

We have reported room-temperature pseudodielectric function data obtained by spectroscopic ellipsometry for $In_xGa_{1-x}As$ alloy films grown on InP substrates. The best surfaces were obtained with a BrM treatment followed by a rinse with 1:5 NH_4OH in methanol. We have also obtained accurate values of the $E_1, E_1+\Delta_1, E_0', E_0'+\Delta_0'$, and E_2 CP energies by analyzing second-energy-derivative line shapes calculated numerically from these data. We developed analytic fits to these data using the parametric semiconductor model, then represented the parameters of this model as quadratic functions of composition x to allow the dielectric functions of $In_xGa_{1-x}As$ alloy films to be obtained for any x. While uncertainties still remain, we believe that improvements will require the use of bulk samples that are not presently available. Until then, our results should be useful in a wide range of applications.

ACKNOWLEDGMENT

This work was supported by the Korea Science and Engineering Foundation through the Quantum Photonic Science Research Center at Hanyang University. This work is also supported by the National Research Laboratory Fund through Compound Semiconductor Epitaxy Laboratory. The work at North Carolina State University was supported by the Office of Naval Research. The work at the Tohoku University was partly supported by the invitation program for foreign researchers to the Venture Business Laboratory of Tohoku University.

*Electronic address: ydkim@khu.ac.kr

[1] L. Geelhaar, R.A. Bartynski, F. Ren, M. Schnoes, and D.N. Buckley, J. Appl. Phys. **80**, 3076 (1996), and references therein.

[2] S.R. Johnson, E. Grassi, M. Beaudoin, M.D. Boonzaayer, K.S. Tsakalis, and Y.H. Zhang, J. Vac. Sci. Technol. B **17**, 1237 (1999), and references therein.

[3] C. Pickering, R.T. Carline, M.T. Emeny, N.S. Garawal, and L.K. Howard, Appl. Phys. Lett. **60**, 2412 (1992).

[4] G.Y. Seong, C.Y. Bang, and Y.D. Kim, J. Korean Phys. Soc. **39**, S389 (2001).

[5] T.J. Kim, Y.S. Ihn, Y.D. Kim, S.J. Kim, D.E. Aspnes, T. Yao, K. Shim, and B.H. Koo, Appl. Phys. Lett. **81**, 2367 (2002).

[6] D.E. Aspnes and A.A. Studna, Appl. Opt. **14**, 220 (1975).

[7] P. Lautenschlager, S. Logothetidis, L. Vina, and M. Cardona, Phys. Rev. B **32**, 3811 (1985).

[8] S. Logothetidis, M. Alouani, M. Garriga, and M. Cardona, Phys.

Rev. B **41**, 2959 (1990).
[9] S.M. Kelso, D.E. Aspnes, M.A. Pollack, and R.E. Nahory, Phys. Rev. B **26**, 6669 (1982).
[10] M. Schubert, V. Gottschalch, C.M. Herzinger, H. Yao, P.G. Snyder, and J.A. Woollam, J. Appl. Phys. **77**, 3416 (1995).
[11] S. Adachi, Phys. Rev. B **35**, 7454 (1987).
[12] Y.D. Kim, M.V. Klein, S.F. Ren, Y.C. Chang, H. Luo, N. Samarth, and J.K. Furdyna, Phys. Rev. B **49**, 7262 (1994).
[13] D.E. Aspnes and A.A. Studna, Phys. Rev. B **27**, 985 (1983).
[14] S.G. Choi, Y.D. Kim, S.D. Yoo, D.E. Aspnes, D.H. Woo, and S.H. Kim, J. Appl. Phys. **87**, 1287 (2000).
[15] Y.D. Kim, S.G. Choi, M.V. Klein, S.D. Yoo, D.E. Aspnes, S.H. Xin, and J.K. Furdyna, Appl. Phys. Lett. **70**, 610 (1997).
[16] B. Johs, C.M. Herzinger, J.H. Dinan, A. Cornfeld, and J.D. Benson, Thin Solid Films **313**, 137 (1998).
[17] T.G. Andersson, Z.G. Chen, V.D. Kulakovskii, A. Uddin, and J.T. Vallin, Appl. Phys. Lett. **51**, 752 (1987).
[18] I.J. Fritz, Appl. Phys. Lett. **51**, 1080 (1987).
[19] D.E. Aspnes and A.A. Studna, Appl. Phys. Lett. **39**, 316 (1981).
[20] Y.D. Kim, S.L. Cooper, M.V. Klein, and B.T. Jonker, Appl. Phys. Lett. **62**, 2387 (1993).
[21] G.E. Jellison, Jr., T.E. Haynes, and H.H. Burke, Opt. Mater. (Amsterdam, Neth.) **2**, 105 (1993).
[22] F.H. Pollak and M. Cardona, Phys. Rev. **172**, 816 (1968).
[23] J.A.V. Vechten and T.K. Bergstresser, Phys. Rev. B **1**, 3351 (1970).
[24] O. Berolo, J. Woolley, and J.A.V. Vechten, Phys. Rev. B **8**, 3794 (1973).
[25] M. Cardona, *Modulation Spectroscopy*, Suppl. 11 of *Solid State Physics*, edited by F. Seitz, D. Turnbell, and H. Ehrenreich (Academic, New York, 1969.)
[26] D. E. Aspnes, in *Handbook on Semiconductors*, edited by M. Balkanski (North Holland, Amsterdam, 1980), Vol. 2, p. 109.
[27] E.W. Williams and V. Rehn, Phys. Rev. **172**, 798 (1968).
[28] L. Vina, C. Umbach, M. Cardona, and L. Vodopyanov, Phys. Rev. B **29**, 6752 (1984).
[29] A.G. Thompson and J.C. Woolley, Can. J. Phys. **45**, 2597 (1967).
[30] G. Burns, *Solid State Physics* (Academic Press Inc., London, 1985), p. 461.
[31] H. Yao, P.G. Snyder, and J.A. Woollam, J. Appl. Phys. **70**, 3261 (1991), and references therein.
[32] F.L. Terry, Jr., J. Appl. Phys. **70**, 409 (1991).
[33] C.C. Kim, J.W. Garland, and P.M. Raccah, Phys. Rev. B **47**, 1876 (1993).
[34] ''Guide to Using WVASE32,'' Software for Spectroscopic Ellipsometry Data Acquisition and Analysis, J. A. Woollam Co., Inc., 2000.
[35] C. M. Herzinger and B. Johs, US Patent No. 5796983, 1998.